Check for updates

A comparative study of W, V, and Co doping in MoSe₂ for high-performance flexible all-solid-state supercapacitors

Pewe-u Marhu and Vijeth H. [ID] *

The importance of supercapacitor electrode materials and devices undoubtedly stands out in relation to energy storage devices. Selecting a suitable electrode material is crucial for characterization and electrochemical studies. Herein, we report a one-step hydrothermal strategy for the fabrication of molybdenum diselenide ($MoSe_2$) and 2% tungsten-, vanadium- and cobalt-doped $MoSe_2$, along with characterization. The structural and morphological changes in the various nanocomposites were confirmed by powder X-ray diffraction, Raman spectroscopy, scanning electron microscopy, transmission electron microscopy, and X-ray photoelectron spectra. Electrochemical studies reveal significant improvement in specific capacitance, with the $Co@MoSe_2$ electrode exhibiting the highest specific capacitance of 518 F g^{-1} at 1 A g^{-1} over a potential window of 0.7 V in 2 M KOH electrolyte solution. The fabricated symmetric supercapacitor device (SSD) delivered a specific capacitance of 127 F g^{-1} at 1 A g^{-1} over a potential window of 1.4 V. It achieved a maximum energy density of 34.54 W h kg^{-1} with a power density of 700 W kg^{-1}. The device demonstrated excellent durability, with cycling stability of 80% even after 10 000 cycles. The results obtained are highly promising, indicating that these materials hold significant potential for commercial applications in energy storage devices.

1. Introduction

Flexible electronics are becoming increasingly prevalent, paving the way for a more comfortable lifestyle for generations to come. There is an increasing demand for energy storage and conversion (ESC) devices with tiny volumes, compact size, superior security, outstanding technical longevity, and excellent electrochemical capabilities. High-performance ESC devices are ideal for powering flexible electronics, particularly multifunctional electronic devices that can monitor, detect, and transmit simultaneously.[1,2] Among ESC devices, supercapacitors stand out as an upgraded technology, receiving increasing attention for their high power density, fast charge–discharge rates, good efficiency, long cycle life, and flexibility. Supercapacitors can be classified into three types based on their charge-storage mechanism, namely (i) electric double-layer capacitors (EDLCs), which utilize carbon-based materials; (ii) pseudocapacitors, which are usually redox-active materials; and (iii) hybrid capacitors, which are a combination of EDLC and pseudo-materials.[3,4] Supercapacitors are now extensively used in a range of applications, particularly those requiring the storage/release of a large quantity of energy in a short period of time. They have recently been used mostly in electric vehicles due to their

superior charge–discharge capacity and ability to perform efficiently over numerous cycles.[5,6] They can be used as a power backup in uninterruptible power supply (UPS) systems, in windmill tracking to smooth out the inconsistent power produced by the wind, and in robotics, to deliver short bursts of power, improving performance during variable tasks. Flexible supercapacitors have also been used in wearable electronics as batteries are too bulky and require a liquid electrolyte. All these qualities make them very appealing for a wide range of applications.[7,8] The electrochemical efficacy of supercapacitors is primarily dependent on the design and synthesis of the electrode materials, making the appropriate selection of electrode materials extremely important.[7] Consequently, transition-metal dichalcogenides (TMDCs) are now being adopted as active electrode materials in supercapacitors owing to their distinctive characteristics, which include a substantial specific surface area, suitable dimensions, good electrical conductivity and thermal and chemical stability. Among several TMDCs, two-dimensional (2D) materials such as molybdenum diselenide ($MoSe_2$) have unique physical and chemical characteristics, such as high specific power, extended stability and cycle life, and enhanced safety profiles, winning out over other electrode materials for use in supercapacitors.[8,9] $MoSe_2$ is a significant material characterized by a substantial layer spacing of 0.65 nm, which reduces the energy barrier for the adsorption and desorption of charged ions.[4,10,11] $MoSe_2$ exhibits two characteristic structural phases: a metallic octahedral 1T phase and

Department of Physics, School of Sciences, Nagaland University (A Central University), Lumami, Nagaland, India-798672. E-mail: vijethhebri@gmail.com; vijeth@nagalanduniversity.ac.in

a semiconducting trigonal prismatic 2H phase. $MoSe_2$ naturally occurs in the 2H phase due to its thermodynamic stability; the 1T phase is metastable and can be reversibly transformed into the 2H phase. Given the robust catalytic activity attributed to the elevated conductivity of 1T-phase $MoSe_2$, phase transition engineering has been identified as an effective method to enhance its electrocatalytic performance.[12] With an unusual atomic structure, three layers of atoms make up $MoSe_2$, and they are stacked and joined by weak van der Waals[13] contacts, with strong covalent bonding within the layers. Consequently, $MoSe_2$ layers are easily separated from the bulk and have been utilized in supercapacitors.[14,15] Gao *et al.* synthesized $MoSe_2$ using a facile hydrothermal method and obtained a specific capacitance of 243 F g^{-1} at 0.5 A g^{-1}, and still kept 90.3% capacitance after 1000 cycles at 1 A g^{-1}.[13] Regardless of the great theoretical capacity, limited electronic conductivity leads to low capacitances. To address this issue, a promising technique is to adorn $MoSe_2$ with highly conductive materials by doping. This offers a key method to alter its properties through the customization of the composition.[16] For instance, Bhat *et al.* prepared W-doped $MoSe_2$/graphene, delivering an enhanced specific capacitance of 248 F g^{-1} which was complimented by excellent capacitance retention capability of 102% for 20 000 cycles.[16] Furthermore, Zhu *et al.* fabricated a supercapacitor device, which delivers a capacitance of 49.7 F g^{-1} and a maximal energy density of 25.3 W h kg^{-1} at a power density of 1143.6 W kg^{-1}.[17] Thus motivated, this study presents a comparative analysis of a pure sample and samples with structural modifications and enhanced electrochemical properties achieved through material doping. Hence, we effectively synthesized molybdenum diselenide ($MoSe_2$) *via* a facile one-step hydrothermal method and investigated the effects of tungsten (W), vanadium (V), and cobalt (Co) doping on its electrochemical performance for supercapacitor applications. The selection of these transition metals was based on their distinct electronic configurations, which can modulate and enhance electrochemical properties. Specifically, tungsten doping is known to improve charge transfer kinetics and stability due to its high oxidation states and strong bonding with chalcogenides. Vanadium's multiple redox states can contribute to pseudocapacitance, increasing specific capacitance. Cobalt's fast redox activity and good electrical conductivity can facilitate faradaic reactions, enhancing energy storage capabilities. A comparative analysis of the structural, morphological, and electrochemical properties of pure and doped $MoSe_2$ samples was conducted to elucidate the impact of doping. The electrochemical results with 2 M KOH as the electrolyte solution in a three-electrode system indicated that the doped $MoSe_2$ electrode had enhanced storage capacity. The results demonstrated significant enhancements, with a 1- to 2-fold increase in specific capacitance compared with the pure sample. Additionally, the development of a novel supercapacitor was examined for symmetric device configurations. A significant enhancement in energy density was observed, with values increasing from 15.49 W h kg^{-1} to 34.54 W h kg^{-1}, representing a substantial improvement and partially achieving one of the desired performance metrics for supercapacitor devices. Furthermore, the flexibility of the supercapacitor device

was also tested, addressing a core obstacle for such devices and demonstrating potential for lightweight, portable, and compatible applications connected with present or next-generation energy storage and cutting-edge devices.

## 2. Experimental section

2.1. Materials

Sodium molybdate dihydrate ($Na_2MoO_4 \cdot 2H_2O$), hydrazine hydrate ($N_2H_4 \cdot H_2O$), sodium tungstate dihydrate ($Na_2WO_4 \cdot 2H_2O$), selenium powder (Se), ammonium metavanadate (NH_4VO_3), and cobalt chloride hexahydrate ($CoCl_2 \cdot 6H_2O$) were purchased from Sigma Aldrich, and were 99% pure.

2.2. Synthesis of $MoSe_2$ and W-, V-, and Co-doped $MoSe_2$

Using the technique of hydrothermal heating, a $MoSe_2$ sample with a 1 : 2 weight ratio is obtained. Specifically, 160 mg of Se in 4 mL of $N_2H_4 \cdot H_2O$ is allowed to age for 24 h, and this is denoted as solution A. Concurrently, 250 mg of $Na_2MoO_4 \cdot 2H_2O$ is dissolved in 55 mL of DIW, which is labelled as solution B. Solution A is then slowly added dropwise into solution B under continuous stirring; a red-colour solution appears. The resulting mixture is transferred to a 100-mL Teflon-lined stainless-steel autoclave and heated at 180 °C for 24 h, followed by cooling to room temperature. The sample is subsequently washed several times with DIW and ethanol with centrifugation. Finally, the sample is allowed to dry at 60 °C overnight. The entire process is illustrated in Scheme 1. To synthesize W- ($Mo_{0.98}Se_2W_{0.02}$), V- ($Mo_{0.98}Se_2V_{0.02}$), and Co-doped ($Mo_{0.98}Se_2Co_{0.02}$) $MoSe_2$, the precursors $Na_2WO_4 \cdot 2H_2O$, NH_4VO_3, and $CoCl_2 \cdot 6H_2O$, respectively, are added, replacing equal molar percentages of $Na_2MoO_4 \cdot 2H_2O$, using the same technique as before (Scheme 1), and these are designated W@$MoSe_2$, V@$MoSe_2$, and Co@$MoSe_2$, accordingly.

2.3. Electrochemical measurements and fabrication of an all-solid-state flexible supercapacitor

To eliminate any potential oxide layer from the surface, a piece of nickel foam (NF) (1 cm × 1.5 cm) was immersed in 3 M HCl solution for 30 min. After multiple ultrasonic cleaning cycles with DI water, acetone, and ethanol, it was dried at room temperature. The active electrode material was prepared by mixing the active material with PVDF, as a binder, and activated charcoal at a mass ratio of 80 : 10 : 10 and grinding the mixture with a mortar and pestle. *N*-Methyl pyrrolidone (NMP) was then added to form a slurry. Following that, the resulting slurry was coated onto clean NF (1 cm × 1 cm) and set aside to dry at 70 °C for 6 h. About 3 mg of active material was coated on each piece of NF. A standard three-electrode electrochemical cell is employed with the prepared electrode, platinum wire, and Ag/AgCl as the working electrode, counter electrode, and reference electrode, respectively, in 2 M KOH solution, as depicted in Scheme 1(b). In a two-electrode system, the SSD was fabricated by sandwiching two identical prepared electrodes, separated by a Whatman filter paper with a thickness of 5 mm, with PVA–KOH gel as the electrolyte, as illustrated in Scheme 1(c). The gel
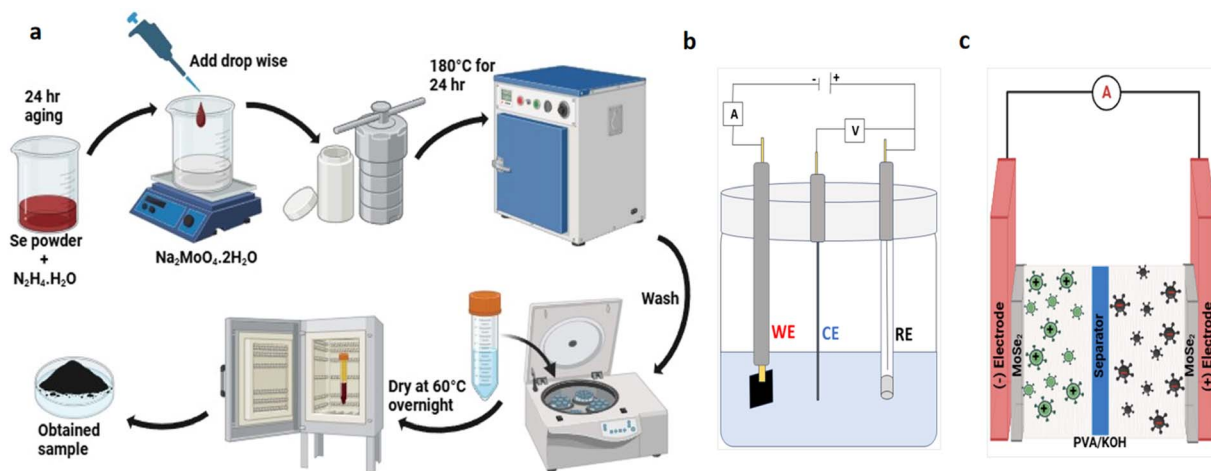
Scheme 1 (a) An illustration of the synthesis procedure for the preparation of powder samples *via* a hydrothermal method, (b) an illustration of the 3-electrode setup and (c) the construction of the symmetric supercapacitor device.

electrolyte was prepared by dissolving 2 g of PVA and 2 g of KOH in 20 mL of DI water separately and stirring for 30 min. These two solutions were mixed together and maintained at 80 °C under vigorous stirring for 2 h. The positive and negative electrodes are constructed with prepared $MoSe_2$, $W@MoSe_2$, $V@MoSe_2$, and $Co@MoSe_2$. Both electrodes, with equal active material loading, had uniform contact with the electrolyte, ensuring effective utilization of the active material and balanced charge transfer during the tests. The electrochemical performance data are evaluated utilizing a Biologic SP-300 electrochemical workstation for cyclic voltammetry (CV), galvanostatic charge–discharge (GCD), and electrochemical impedance spectroscopy (EIS). The specific capacitance is calculated using eqn (1):[18]

$$C = \frac{I \, dt}{m \, dV} \tag{1}$$

where, I is the current, dt is the discharge time, m is the active mass, dV is the potential range, and C indicates the specific capacitance.

The energy density (E, W h kg^{-1}) and power density (P, W kg^{-1}) of the assembled SSD are calculated as follows:

$$E = \frac{CV^2}{7.2} \tag{2}$$

$$P = \frac{E \times 3600}{dt} \tag{3}$$

where V is the voltage window, E represents the energy density, and P is the power density.

3. Results and discussion

3.1. Structural and morphological studies

Verification of the condition and phase of the synthesized material has been accomplished using PXRD. Fig. 1(a) shows peaks at 2θ angles of 13.38°, 33.49°, 41.48°, 54.98°, and 65.54°, which correspond to the (002), (102), (006), (110), and (200)

crystal planes of $MoSe_2$, respectively, and are matched with JCPDS no. 29-0914. The reaction equation, based on the above discussion, is given below:

$$Mo + 2Se + N_2H_4 \cdot H_2O \rightarrow MoSe_2 + N_2 + 2H_2O \tag{4}$$

The PXRD patterns of the $W@MoSe_2$, $Co@MoSe_2$, and $V@MoSe_2$ nanostructures show comparable peaks to those of pure $MoSe_2$ with enhanced peak intensities, despite the presence of a weak Se ring (*) and a small shift in the 2θ positions to the left.[16] Additionally, $MoSe_2$ peaks are visible at angles of 27° and 56° for the (004) and (008) planes in the PXRD patterns of the doped nanostructures. These findings show that transition metals have been successfully doped into the host lattice and that crystallinity has increased. Fig. 1(b) shows refinement conducted on the pure sample, and the low chi-square value of 1.08 indicates the goodness of fit. The development of nanostructured multilayer $MoSe_2$ is seen in the PXRD patterns, which display a hexagonal phase of $MoSe_2$ with a space group of $P6_3/mmc$.[19] According to the Debye–Scherrer equation given below, the average crystallite size of $MoSe_2$ was determined to be 2 nm:

$$D = k\lambda/\beta \cos\theta \tag{5}$$

where the crystallite size D is measured in nanometers, the constant k is equal to 0.94, the material's wavelength λ is equal to 0.15 nm, the line expansion, β (FWHM), is the full width at half maximum in radians, and the Bragg angle is indicated by θ. PXRD analysis indicates an enhancement in the electrochemical performance by revealing a balanced crystalline peak pattern, resulting in structural stability and better conductivity with improved ionic transport pathways. The synthesis of $MoSe_2$ was further verified using Raman spectroscopy, as shown in Fig. 1(c). Two separate $MoSe_2$ peaks can be found in the spectrum at about 237.85 and 284.86 cm^{-1}. These peaks correspond to the out-of-plane A_{1g} and in-plane E_{2g}^1 vibrational
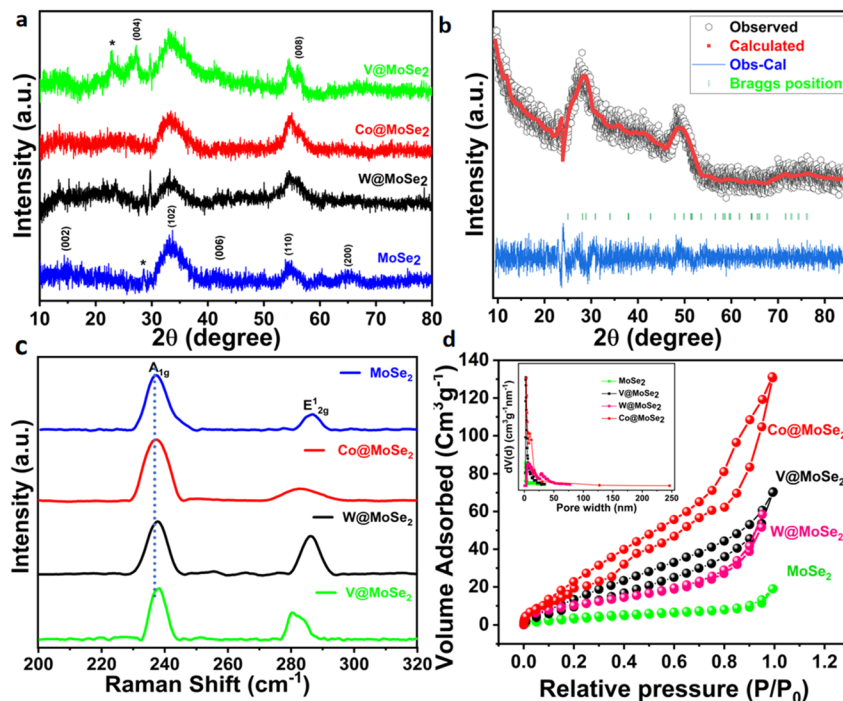
Fig. 1 (a) Powder X-ray diffraction (PXRD) patterns of a pure $MoSe_2$ sample, $W@MoSe_2$, $Co@MoSe_2$ and $V@MoSe_2$. (b) Rietveld refinement performed on the XRD data of a pure $MoSe_2$ sample. (c) Raman spectra of $MoSe_2$, $W@MoSe_2$, $Co@MoSe_2$, and $V@MoSe_2$. (d) BET results and the corresponding BJH plots (inset).

modes. Furthermore, the Raman spectra of $W@MoSe_2$, $Co@MoSe_2$, and $V@MoSe_2$ nanostructures show a minor shift to the right, demonstrating successful integration *via* $MoSe_2$ doping. This leads to improved electrochemical adaptability and more active sites for the charge-storage mechanism. The Brunauer–Emmett–Teller (BET) technique was employed to determine the specific surface areas and average pore volumes of the synthesized materials, as illustrated in Fig. 1(d). The analysis revealed that the $Co@MoSe_2$ sample exhibited the highest surface area of 113.03 m^2 g^{-1} with a corresponding pore volume of 0.21 cm^3 g^{-1}. In comparison, the $V@MoSe_2$ and $W@MoSe_2$ samples showed moderate surface areas of 51.6 m^2 g^{-1} and 50.2 m^2 g^{-1}, respectively, with pore volumes of 0.18 cm^3 g^{-1} and 0.11 cm^3 g^{-1}, respectively. The pristine $MoSe_2$ sample displayed the lowest surface area and pore volume, measured at 13.9 m^2 g^{-1} and 0.03 cm^3 g^{-1}, respectively. The BET analysis confirms that the incorporation of Co, V, and W atoms into the $MoSe_2$ matrix *via* hydrothermal synthesis occurs through substitutional doping at Mo sites. This atomic substitution induces a redistribution of electronic density, increases the density of electrochemically active sites, and strengthens the interactions among chemical bonds within the host lattice. These structural and electronic modifications collectively enhance the electrochemical performance of the electrode material. Moreover, the mesoporous frameworks of the doped samples facilitate improved electrolyte ion diffusion and maximize the electrode–electrolyte interfacial contact area, thereby contributing to superior charge-storage characteristics.[20] Fig. 2 shows magnified FESEM images of $MoSe_2$ and

doped materials, indicating that they are laminated with varying sizes heaped together. Some nanorods with average diameters of 55 nm are also detected, along with nanoflowers assembled from ultra-thin nanosheets that tend to congregate and overlap with each other, as illustrated in the HRTEM image (Fig. 3) of $MoSe_2$.[10,16,19] This indicates time-dependent nanostructure growth with a subsequent increase in surface coverage by 3D nanoflower-like structures.[21] As seen in Fig. 2(a), pristine $MoSe_2$ exhibits a flower-like morphology composed of agglomerated nanoparticles and occasional nanorods (~42–58 nm). These features facilitate the formation of interconnected porous networks, offering enhanced ion accessibility and diffusion channels. In the case of $V@MoSe_2$ (Fig. 2(b)), the morphology evolves into larger spherical aggregates with particle sizes ranging from approximately 45 to 75 nm. This increase in particle size and surface roughness suggests enhanced nucleation and growth mechanisms during synthesis, potentially improving interactions between the electrode surface and the electrolyte, though it may slightly reduce overall porosity. For $W@MoSe_2$ (Fig. 2(c)), the sample exhibits a denser structure, with prominent nanorods (~47–60 nm) intertwined within the matrix. The presence of these rod-like features indicates a more ordered structural arrangement, which could facilitate improved electron transport and contribute to greater mechanical stability. The $Co@MoSe_2$ sample (Fig. 2(d)) reveals a loosely packed configuration characterized by a mixture of thin nanorods and a sheet-like texture, with feature sizes in the range of 58–76 nm. This porous and layered morphology is likely to enhance the effective surface area and expose more
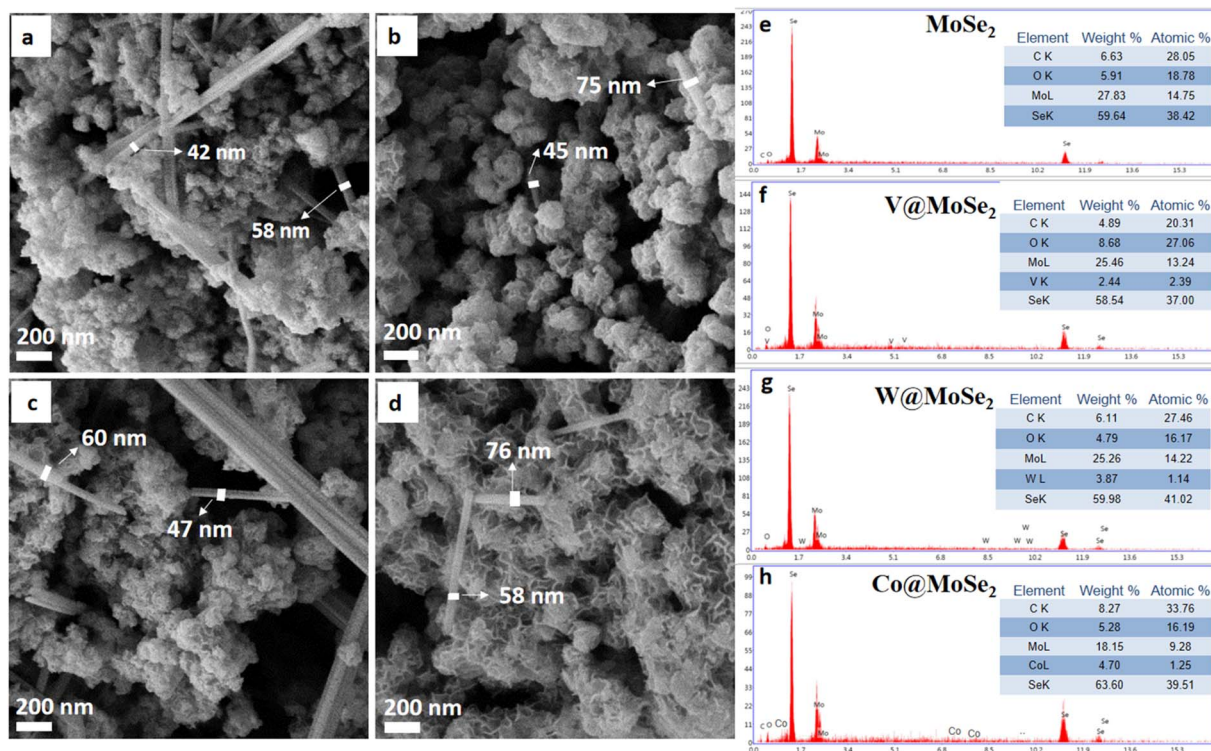
Fig. 2 FESEM images of (a) MoSe$_2$, (b) V@MoSe$_2$, (c) W@MoSe$_2$, and (d) Co@MoSe$_2$, and (e–h) EDX spectra confirming the elemental compositions of the samples.
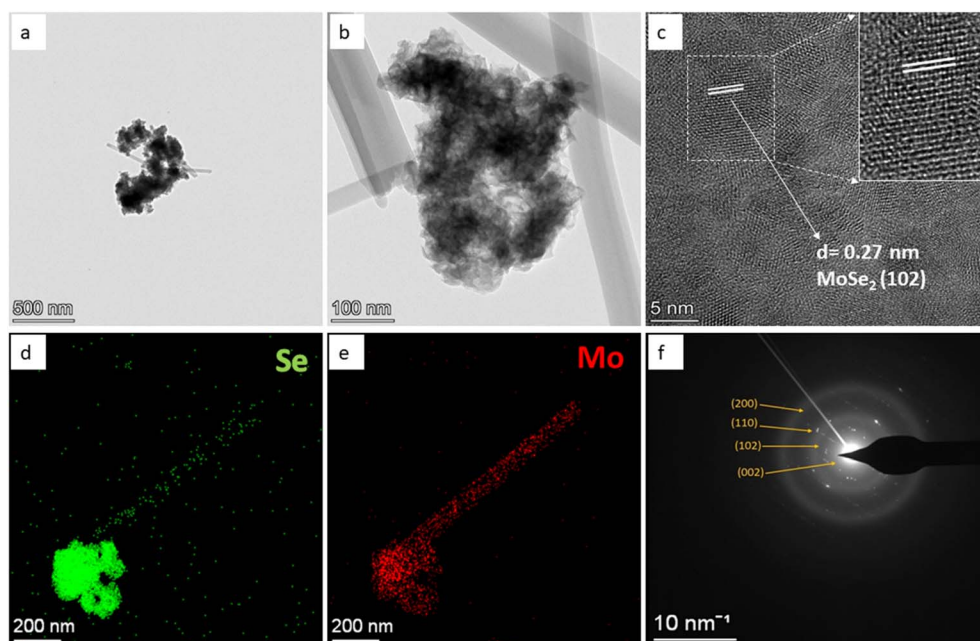

Fig. 3 (a–c) HRTEM images of a pure sample, (d and e) element mapping of Mo and Se, and (f) the SAED pattern of MoSe$_2$.

electroactive sites, thereby promoting better ion diffusion and charge-storage capabilities. These findings suggest that while the nanoflower structure of MoSe$_2$ is generally retained across all doped samples, each dopant undergoes unique morphological transformations that directly influence the material's

surface area, porosity, and electrochemical properties. In addition, as shown in Fig. 2(b)–(d), FESEM examinations of the doped samples demonstrate that minimal doping of the pure sample does not alter the morphology but results in increased size and reduction in agglomeration. This confirms the effective

growth of rod- and sheet-like nanostructures on $MoSe_2$, which present a larger surface to the electrolyte, create more active sites and allow ions to rapidly move into and out of the material.[22] This results in an increased surface area and more active sites, with electrochemical performance showing better capacitance and rate performance. HRTEM measurements, as shown in Fig. 3(a)–(f), present nanosheets of the as-synthesized $MoSe_2$, which closely match the observations from FESEM study. The interplanar spacing of $MoSe_2$ in Fig. 3(c) is 0.27 nm, from the (102) plane, indicating the polycrystalline nature of the material. Fig. 3(d) and (e) depicts the individual proportions of homogeneous Mo and Se elements over the designated area, with the distributions indicated in red and green, respectively. The rings in Fig. 3(f), indexed to the (002), (102), (110) and (200) planes, correspond to $MoSe_2$ and are in good agreement with the XRD results.[10,21,22] XPS analysis was performed to investigate the chemical states and confirm the successful doping of the pristine sample. The deconvoluted Mo 3d spectrum is displayed in Fig. 4(a), where two prominent peaks are visible at binding energies of around 228.14 and 231.27 eV, which correspond to $3d_{5/2}$ and $3d_{3/2}$ Mo^{4+} states, respectively.[23] Minor shoulders at higher binding energies may indicate slight oxidation (Mo^{6+}), possibly due to surface exposure. The oxidation state of the selenium (Se^{2-}) is indicated by the two deconvoluted peaks in the Se 3d plot in Fig. 4(b) at binding energies of 53.49 and 54.38 eV, showing Se $3d_{5/2}$ and Se $3d_{3/2}$, respectively.[24] Bulk sp^3-bonded C–C carbon appears at 285.05 eV in the C 1s profile in Fig. 4(c). Similarly, Fig. 4(d) shows the W 4f spectrum, displaying doublet peaks at ~35.6 eV (W $4f_{7/2}$) and ~37.7 eV (W $4f_{5/2}$), corresponding to W^{6+} species, and indicating that W likely

substitutes Mo in the lattice while preserving the structural integrity of $MoSe_2$. The W^{6+} state is known to influence electrical conductivity and increase the active surface area.[19] The formation of V–Se bonds is responsible for the V $2p_{1/2}$ and $2p_{3/2}$ peaks corresponding to V^{4+}/V^{5+} oxidation states, which are located at 520.03 and 512.45 eV, respectively. The coexistence of multiple valence states suggests the potential for battery behavior due to reversible surface redox reactions. This confirms that $MoSe_2$ was successfully doped with V atoms (Fig. 4(e)). The presence of Co^{2+}/Co^{3+}, likely substituted into Mo sites or present in interstitial positions and contributing to enhanced electrochemical activity *via* redox reactions, is indicated by the peaks at 777.64 and 792.41 eV, which are attributed to the electron-binding energies of Co $2p_{3/2}$ and Co $2p_{1/2}$, respectively, as seen in Fig. 4(f).[22] These dopants likely create additional electroactive sites and modulate the electronic structure, thereby enhancing charge transport and boosting the overall electrochemical performance.

3.2. Electrochemical analysis

Three-electrode electrochemical tests were carried out to explain the electrochemical storage properties of the fabricated electrodes, as described above in the experimental section. The specific capacity of the electrodes is obtained from the CV profiles using the relationship:[25]

$$C_p = \frac{\int I(V)\,dV}{3.6 \times v \times m} \tag{6}$$

where C_p is the specific capacity (mA h g^{-1}) of the electrode, $\int I(V)\,dV$ is the area under the CV curve, v is the scan rate (mV
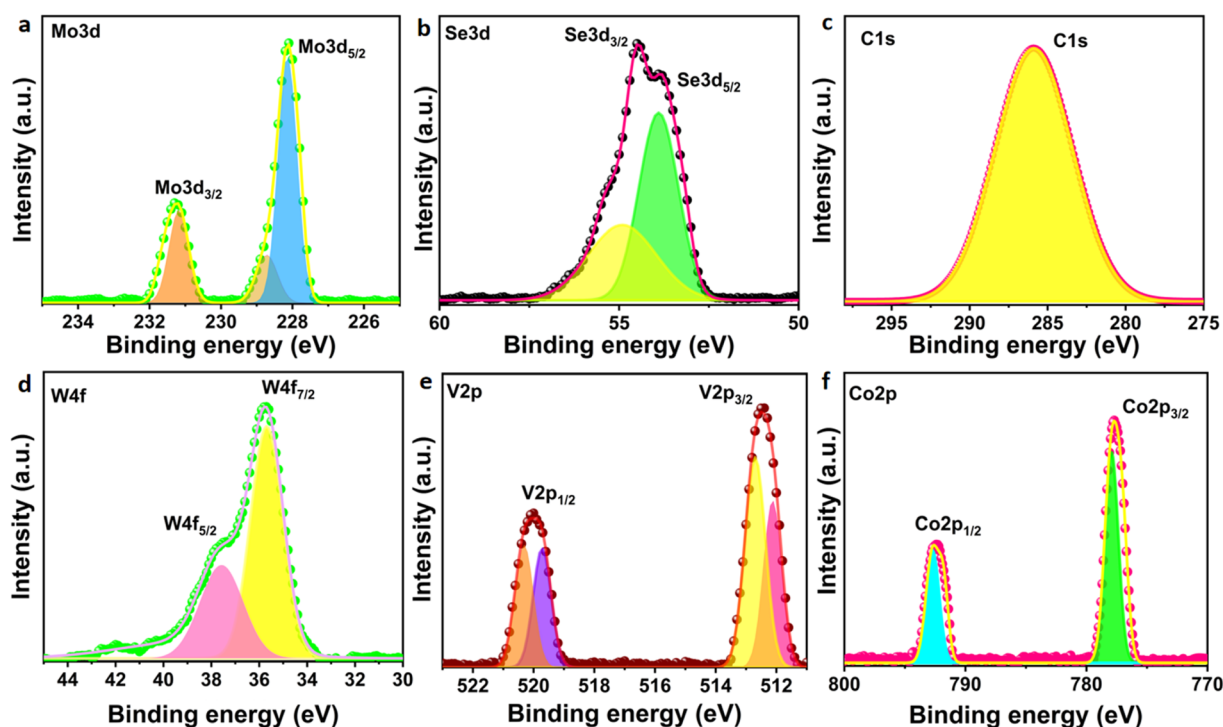

Fig. 4 XPS high-resolution core-level deconvoluted spectra: (a) Mo 3d, (b) Se 3d, (c) C 1s, (d) W 4f, (e) V 2p and (f) Co 2p.
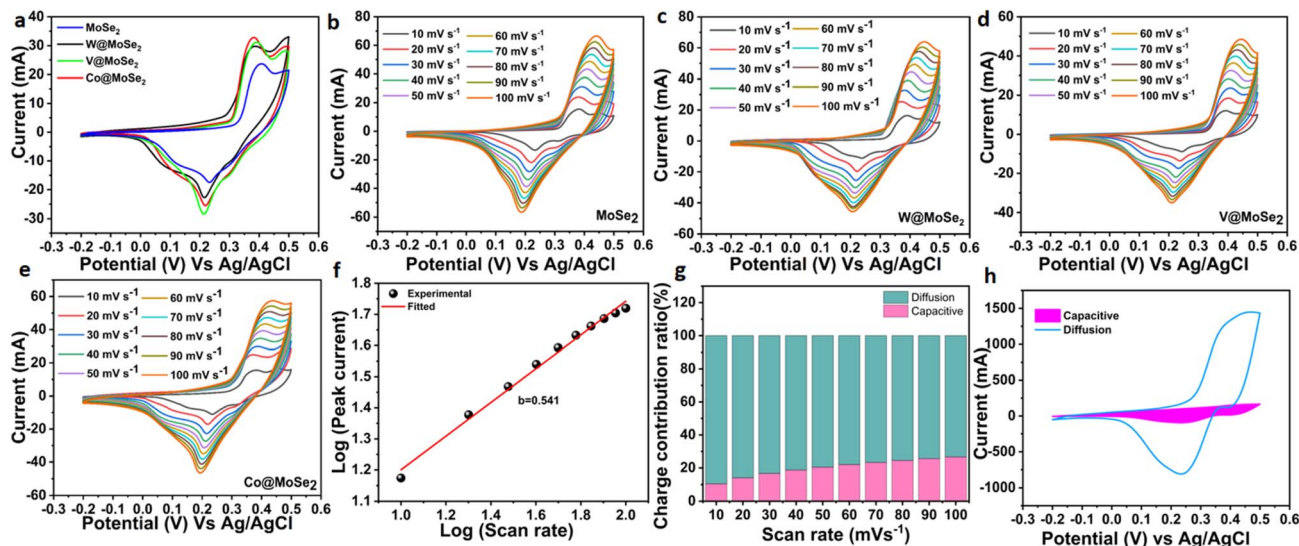
Fig. 5 Three-electrode mode: (a) comparative CV plots at a constant scan rate of 10 mV s^{-1} for all samples, (b–e) CV plots for MoSe$_2$, W@MoSe$_2$, V@MoSe$_2$, and Co@MoSe$_2$ at varied scan rates of 10–100 mV s^{-1}, (f) a b-value estimation of the CoMo@Se$_2$ electrode from a plot of log(peak current) against log(scan rate), (g) the diffusion and capacitive current contributions at scan rates from 10–100 mV s^{-1}, and (h) a CV curve of the Co@MoSe$_2$ material depicting the capacitive/diffusive current contributions at 100 mV s^{-1}.

s^{-1}), and m is the active mass (g). Fig. 5(a) shows the CV curves at 10 mV s^{-1} over a potential window of −0.2 to 0.5 V for MoSe$_2$, W@MoSe$_2$, V@MoSe$_2$, and Co@MoSe$_2$, which have specific capacities of 77.05, 103.10, 107.58 and 113.09 mA h g^{-1}, respectively. The redox couplings of MoSe$_2$ electrodes are investigated, which demonstrate battery properties due to the electrochemical storage mechanism. The Co@MoSe$_2$ electrode has a higher area under the curve, whereas W@MoSe$_2$ and V@MoSe$_2$ also exhibit more catalytic edge sites with rapid conductance behavior, resulting in better electrodes than the bare MoSe$_2$ electrode. The observed large redox profiles could be derived from the involvement of distinct Mo atom valence states.[26] Fig. 5(b)–(e) displays the CV curves for all the prepared electrodes as the scan rate changes from 10 to 100 mV s^{-1}. These images show the intensification of the scan rate and the expansion of the area associated with the CV curve. The results support both the enhanced rate performance and current capabilities of the electrodes. Both the negative and positive versions of the CV curve exhibit symmetry. The fact that the peak current changes in direct proportion to the increase in scan rate suggests that the energy storage mechanism at the electrode/electrolyte interface is highly reversible. The capacitive effect of an electrode material can be analyzed using the CV profiles measured at different scan rates according to the following power law:

$$i = av^b \tag{7}$$

where v is the scan rate (mV s^{-1}) and a and b are adjustable parameters. The b value can be calculated from the slope of log i vs. log v, as shown in Fig. 5(f). There are two boundary conditions: (i) $b = 0.5$ indicates a diffusion-controlled process due to ion intercalation/de-intercalation; and (ii) $b = 1$ represents a surface capacitive nature. The value for the Co@MoSe$_2$

electrode is found to be 0.54 from the log(i) vs. log(v) plot, indicating that the charge-storage mechanism is predominantly diffusion-controlled, which is characteristic of battery-type behavior. However, slight deviations in the CV profile at higher scan rates suggest a minor pseudocapacitive contribution. These surface-related processes, while not dominant, can facilitate faster ion/electron transport, thereby enhancing the rate capability and supporting fast-charging performance. This synergistic behavior is advantageous for high-power applications where both energy density and charge/discharge speed are critical. It is shown that the capacitive route influences charge storage on the Co@MoSe$_2$ electrode, while diffusion processes dominate the storage process. The current value at a specific scan rate (v) and potential (V) can be divided between surface-controlled (k_1v) and diffusion-driven ($k_2v^{1/2}$) reactions as follows:[24,25]

$$I(V) = k_1v + k_2V^{1/2} \tag{8}$$

The values of k_1 and k_2 are obtained through CV analysis at varying scan rates (10–100 mV s^{-1}). The contributions of capacitive and diffusion-controlled processes to the overall electrochemical response were quantified, revealing a small shift towards capacitive dominance at higher scan rates, as shown in Fig. 5(g). As anticipated, because of the shorter time for ion diffusion at higher sweep speeds, the capacitive contribution gradually rises with scan rate. Even though diffusion processes predominate, the growing surface-controlled contribution at high scan rates points to the existence of pseudocapacitive behavior. Fig. 5(h) presents the capacitive contribution at a representative scan rate, where the surface-controlled current is highlighted. The claim that capacitive effects are active and grow more noticeable at high rates is supported by
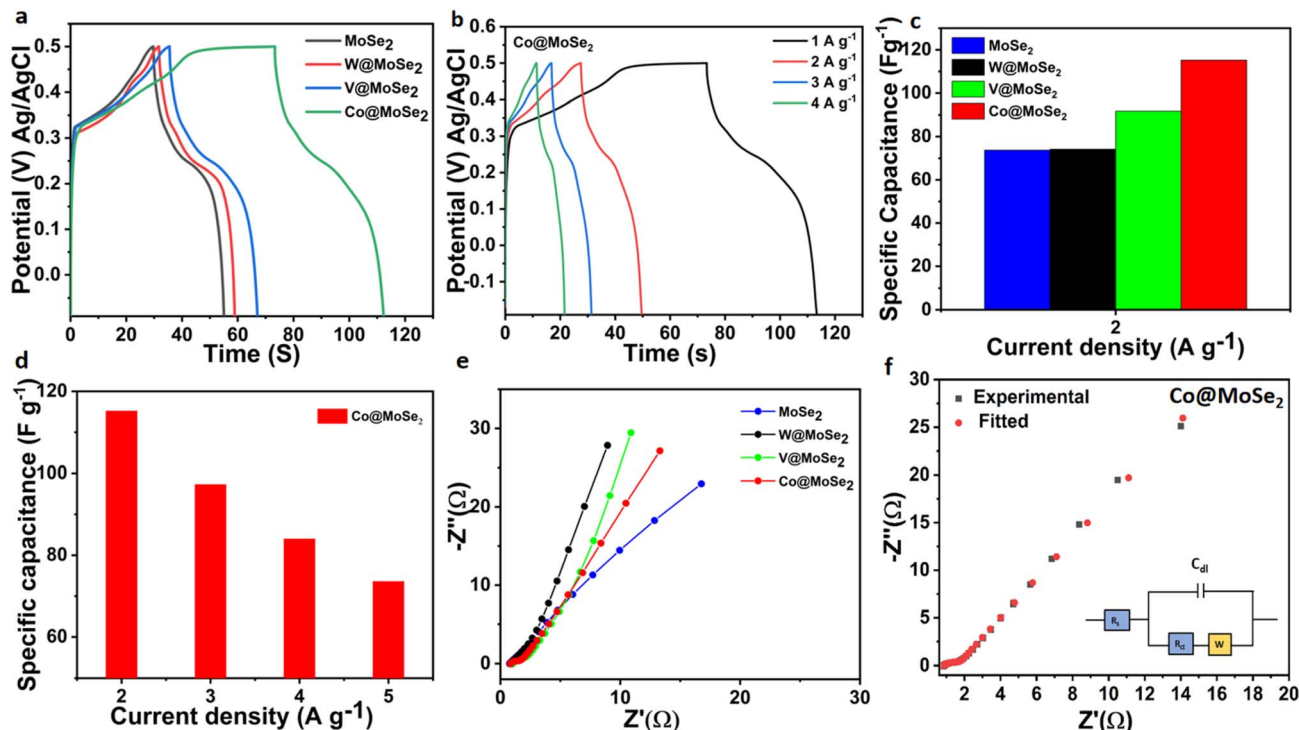
Fig. 6 (a) GCD plots for all samples at 1 A g^{-1}, (b) GCD plots of Co@MoSe$_2$ at varied current densities (A g^{-1}), (c and d) current density *vs.* specific capacitance plots, (e) Nyquist plots corresponding to all prepared samples, and (f) experimental and fitted data for Co@MoSe$_2$ (the inset displays the equivalent fitted circuit).
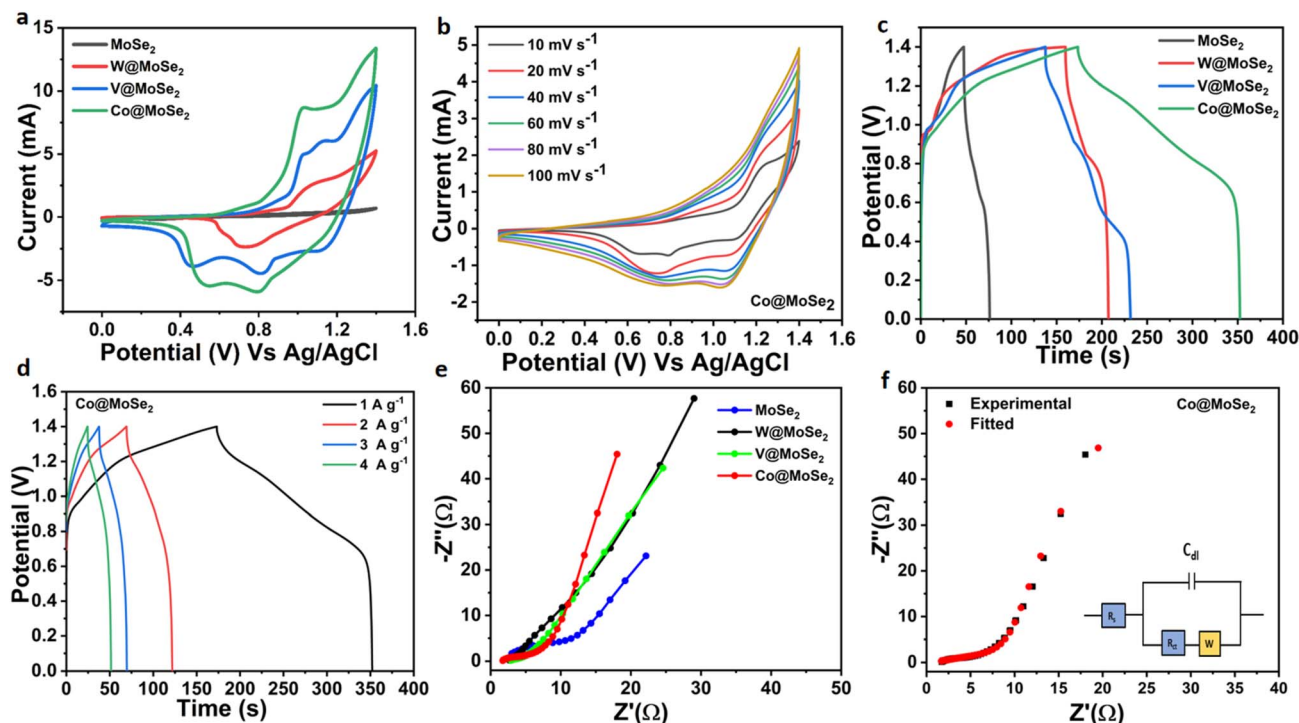

Fig. 7 Device mode: (a) comparative CV plots at a constant scan rate of 10 mV s^{-1} for all samples, (b) CV plots for Co@MoSe$_2$ at varied scan rates (10–100 mV s^{-1}), (c) GCD plots for all samples at a current density of 1 A g^{-1}, (d) GCD plots of Co@MoSe$_2$ at current densities of 1, 2, 3, and 4 A g^{-1}, (e) Nyquist plots corresponding to all prepared samples, and (f) Nyquist plots for Co@MoSe$_2$ using both the experimental and fitted data (inset displays the equivalent fitted circuit).

this, even though diffusion controls the overall charge-storage process. Taken together, our findings show that Co@MoSe$_2$ has a synergistic charge-storage mechanism. Fig. 6(a) shows the generated GCD curves over a potential range of −0.2 to 0.5 V for MoSe$_2$, W@MoSe$_2$, V@MoSe$_2$, and Co@MoSe$_2$ electrodes, which have specific capacitances of 331.71, 372.34, 412.71, and 518.4 F g^{-1} at 1 A g^{-1}, respectively. All electrodes display nonlinear charge/discharge curves due to their battery-like electrochemical storage properties. The extended charging/discharging duration for the Co@MoSe$_2$ electrode is consistent with its high capacitance value and matches the corresponding CV results.[27] The GCD curves further highlight that doping significantly enhances the charge-storage capability of MoSe$_2$. Specifically, V@MoSe$_2$ increases the capacitance by improving charge carrier density and reducing internal resistance, as reflected in its lower R_{ct} value (1 Ω). W@MoSe$_2$, though not as effective as V or Co, also contributes to improved charge transport, likely due to a modified electronic structure and increased conductivity. Co@MoSe$_2$ demonstrates the most remarkable improvement, suggesting the presence of additional redox-active centers (Co^{2+}/Co^{3+}) that may provide pseudocapacitive contributions beyond the electric double-layer mechanism. Fig. 6(b) displays the GCD curves of Co@MoSe$_2$ at different current densities. The calculated specific capacitances were 518.4, 389.14, 315, and 264.83 F g^{-1} at 1, 2, 3, and 4 A g^{-1}, respectively, with plots of current density *versus* specific capacitance presented in Fig. 6(c)–(d). The gradual decrease in capacitance with increasing current density is expected and indicates good rate capability. Nyquist plots for all four electrodes are shown in Fig. 6(e), collectively affirming that doping significantly influences the electrochemical characteristics of MoSe$_2$. The dopants modify the electronic environment and surface reactivity of MoSe$_2$, and the bulk resistance (R_b) values for MoSe$_2$, W@MoSe$_2$, V@MoSe$_2$, and Co@MoSe$_2$ are determined to be 0.9, 1.1, 0.9, and 0.8 Ω, respectively, while the charge transfer resistance (R_{ct}) values are 1.4, 1.3, 1.0, and 0.6 Ω, respectively. The low R_b and R_{ct} values across all samples confirm facile ionic movement and electron transport. Among them, Co@MoSe$_2$ demonstrates the lowest R_{ct}, indicating it has the most efficient interfacial charge transfer kinetics. Fig. 6(f) depicts the experimental and fitted EIS data for Co@MoSe$_2$, using Zsim software. The inset shows the equivalent circuit [$R_b(QR_{ct}W)C$], where Q represents a constant phase element accounting for surface irregularities and non-ideal capacitive behavior. The low impedance response and good fitting support the superior electrochemical behavior of the Co-doped electrode. These results point to reduced resistance and enhanced

charge storage. Among all the samples, Co@MoSe$_2$ appears to be the most beneficial due to its ability to introduce additional active sites and improve electron mobility, which is directly reflected in its high specific capacitance and low impedance parameters. Fig. 7(a) displays CV scans from assembled SSDs using pure MoSe$_2$, W@MoSe$_2$, V@MoSe$_2$, and Co@MoSe$_2$ electrodes at 10 mV s^{-1}. As observed in the three-electrode system, Co@MoSe$_2$ still holds an advantage in terms of a SSD, exhibiting large-area CV curves and a high capacity compared with the other devices. The observed Co@MoSe$_2$ (Fig. 7(b)) CV current increases with increasing sweep rate, confirming the high-rate capability of the designed symmetric device. Furthermore, the observed CV curves maintain their shape throughout cycling, demonstrating the device's excellent storage kinetics and reversible performance. Fig. 7(c) presents the GCD curves of the fabricated SSDs within a voltage window of 0 to 1.4 V, showing specific capacitances of 56.92, 70.99, 81.60 and 127 F g^{-1} at a current density of 1 A g^{-1} for MoSe$_2$, W@MoSe$_2$, V@MoSe$_2$ and Co@MoSe$_2$, respectively. Among these, the Co@MoSe$_2$ SSD produces the optimal storage capacitances of 127, 79.37, 74.91, and 68.57 F g^{-1} at 1, 2, 3 and 4 A g^{-1}, respectively, as observed in the GCD plots in Fig. 7(d). The specific capacitances of all prepared electrodes are higher than those of the devices due to the ideal and isolated conditions of the electrodes. The nonlinear profiles clearly indicate the prolonged charge/discharge span for the devices, and the electrochemical performance of Co@MoSe$_2$ is detailed in Table 1. The energy densities are calculated to be 15.49, 19.32, 22.21, and 34.54 W h kg^{-1} for MoSe$_2$, W@MoSe$_2$, V@MoSe$_2$ and Co@MoSe$_2$, respectively, with Co@MoSe$_2$ having a power density of 700 W kg^{-1}. Fig. 7(e) shows Nyquist plots for all the fabricated devices, where the R_{ct} values are calculated to be 2.5, 2, 1.8 and 1.6 Ω for MoSe$_2$, W@MoSe$_2$, V@MoSe$_2$ and Co@MoSe$_2$, respectively. Additionally, the common PVA–KOH gel electrolyte used in all devices was evaluated using eqn (9):

$$\sigma = \frac{L}{R_b \times A} \qquad (9)$$

where σ is the ionic conductivity (S cm^{-1}), L is the thickness of the gel (cm), R_b is the bulk resistance (Ω), and A is the cross-sectional area of contact (in cm^2). The ionic conductivity was calculated to be 0.0188 S cm^{-1}, confirming good ionic transport in the gel matrix. The experimental and fitted data for Co@MoSe$_2$ are displayed in Fig. 7(f), based on Zsim software, with the inset showing the equivalent circuit. The energy density and power density were assessed using the Ragone plot in Fig. 8(a). Certainly, our SSD acquires a considerably higher

Table 1 The electrochemical performance parameters of the Co@MoSe$_2$-based SSD

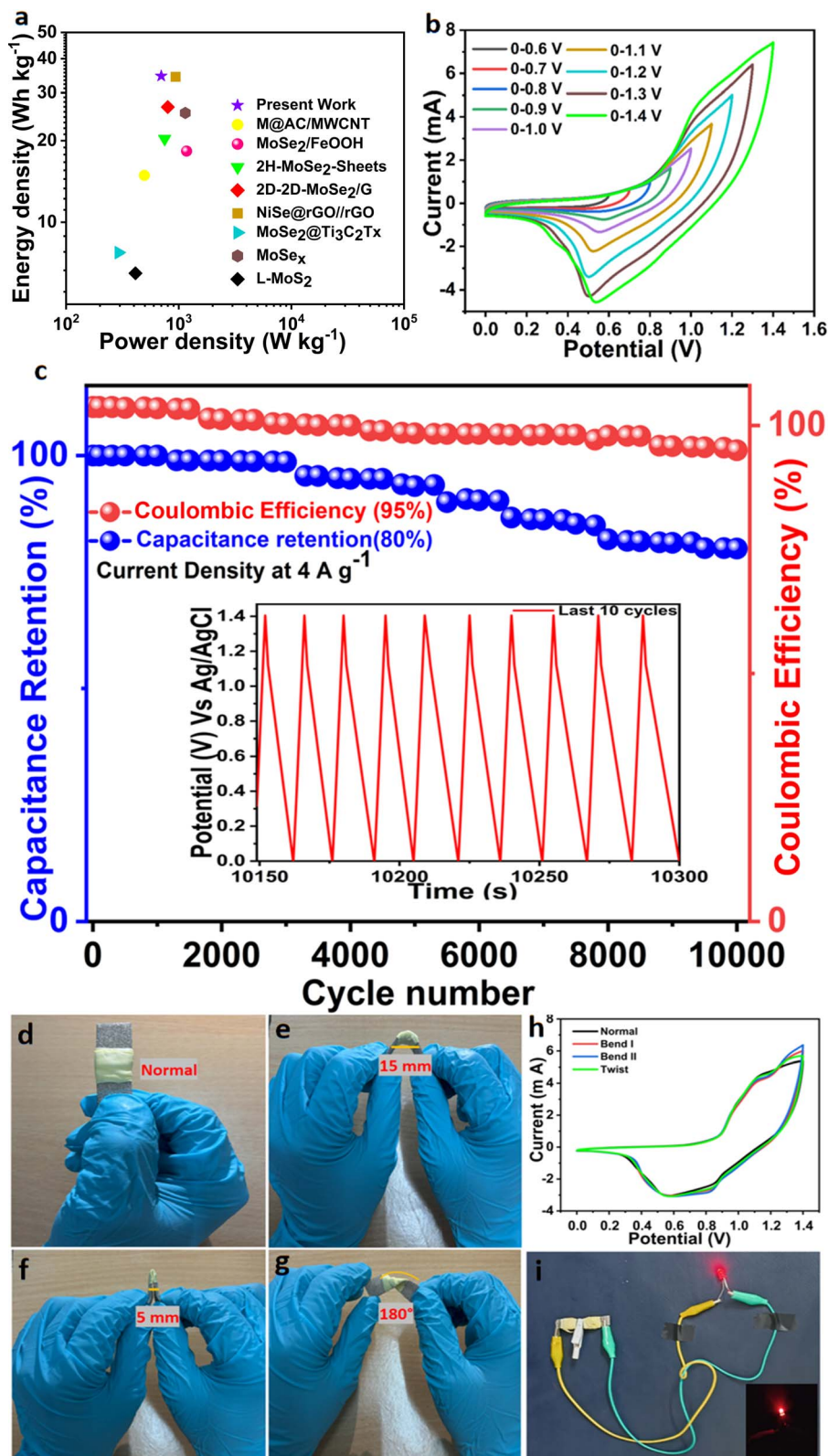| Current density (A g^{-1})	Specific capacitance (F g^{-1})	Energy density (W h kg^{-1})	Power density (W kg^{-1})
1	127	34.54	700
2	79.37	21.6	1413
3	74.91	20.39	2099
4	68.57	18.66	2799

Fig. 8 (a) Ragone plot of the device compared with the reported literature, (b) CV curves observed over different potential windows, (c) cycling stability and coulombic efficiency of the Co@MoSe$_2$ SSD at a current density of 4 A g^{-1} (the inset shows the GCD curves from the last ten cycles), (d–g) pictorial illustrations of the bending and twisting of the SSD and (h) related CV curves, and (i) photographic evidence of a red LED being lit by SSDs in series.

Table 2 An electrochemical performance comparison with literature examples

Sample	Method	Morphology	Electrolyte	Specific capacitance (F g⁻¹)	Energy density (W h kg⁻¹)	Power density (W kg⁻¹)	Cycling stability/cycles	Reference
M@AC/MWCNT	Hydrothermal	Nanoflower	6 M KOH	$133\ (1\ A\ g^{-1})$	14.9	496	86.6% for 10 000 cycles	19
MoSe$_2$/FeOOH	Hydrothermal	Nanorod	6 M KOH	$132\ (1\ A\ g^{-1})$	18.3	1174	100% for 3000 cycles	24
2H-MoSe$_2$-sheets	Hydrothermal	Sheets	0.5 M TEABF$_4$/AN	$16.2\ (0.75\ A\ g^{-1})$	20.31	750	87% for 10 000 cycles	27
2D-2D-MoSe$_2$/N G	Solvothermal	Nanosheets	6 M KOH	$75\ (1\ A\ g^{-1})$	26.6	800	88% for 3000 cycles	28
NiSe@rGO/rGO	Hydrothermal	Sphere	2 M KOH	$115\ (1\ A\ g^{-1})$	34.3	937	93% for 6500 cycles	29
MoSe$_2$@Ti$_3$C$_2$T$_x$	Hydrothermal	Nanoflower	3 M KOH	$223.12\ (1\ A\ g^{-1})$	7.74	292.60	98.69 for 10 000 cycles	30
MoSe$_x$	Electrode deposition	Nanosheets	3 M KOH	$49.7\ (1\ A\ g^{-1})$	25.3	1143.6	50.1% for 10 000 cycles	17
L-MoS$_2$	Hydrothermal	Nanoflowers	2 M KOH	$356.7\ (1\ A\ g^{-1})$	6.5	413	79.6% for 3000 cycles	31
Co@MoSe$_2$	Hydrothermal		2 M KOH	$127\ (1\ A\ g^{-1})$	34.54	700		Present work

energy density, outperforming similar reported transition-metal chalcogenides in other studies, as statistically summarized in Table 2. CV profiles are obtained in various potential windows spanning from 0–0.6 V to 0–1.4 V (Fig. 8(b)) in which the potential steps confirm the faradaic behaviour of the device. At a fixed current density of 4 A g^{-1} (Fig. 8(c)), 80% cyclic stability was demonstrated even after 10 000 GCD cycles, and 95% coulombic efficiency is also achieved. The cycling stability of a SSD is crucial for commercially viable applications. To assess the material's flexibility, it underwent several bending cycles (∼15–5 mm) and manual twisting (∼180°) under various types of mechanical deformation to assess its flexibility and structural integrity; there were no signs of fracturing, as observed in Fig. 8(d)–(g), and the CV curves of the SSD measured at a scan rate of 10 mV s^{-1} within a potential window of 0–1.4 V, as presented in Fig. 8(h), remarkably remain virtually unchanged, maintaining exceptional flexibility and stability even under such conditions, highlighting the superior performance for energy storage applications and reaffirming the robustness for practical applications. Fig. 8(i) shows a photograph demonstrating the successful illumination of a red LED powered by two SSDs connected in series. This proves the practical energy output of the device, showing its ability to power low-voltage electronics and emphasizing the potential of such flexible energy storage systems for use in portable technologies.

4. Conclusions

In a nutshell, we successfully synthesized and fabricated MoSe$_2$, W@MoSe$_2$, V@MoSe$_2$ and Co@MoSe$_2$. Structural analysis using PXRD, Raman, and XPS techniques strongly confirmed the MoSe$_2$ nanostructures. The nanoflower-cum-nanorod structures with dopants were precisely captured by FESEM micrographs and have shown improved surface areas and charge-storage mechanisms. HRTEM investigations explored the expanded layer spacing compared with the pure MoSe$_2$ sample for samples doped with transition metals. The highest electrochemical performance among the prepared samples was achieved by Co@MoSe$_2$, while the other dopants also demonstrated improved performance compared to the pure sample, which is due to the strong synergistic interaction between MoSe$_2$ and the dopants for energy storage. A high specific capacitance of 518 F g^{-1} shows the enhanced electrochemical properties of Co@MoSe$_2$, which are attributed to the large-area CV curves and improved conductive pathways. Building on the promising results from the Co@MoSe$_2$ electrode, a SSD was fabricated, yielding a specific capacitance of 127 F g^{-1}, an energy density of 34.54 W h kg^{-1}, and a power density of 700 W kg^{-1}, displaying extremely superior capacitance retention of 80% of the initial capacity even after 10 000 cycles. The nanostructures of the prepared samples exhibited robust battery-like kinetics during the charge-storage process in a basic medium. Flexibility studies proved that there was no distortion after multiple bending and twisting cycles, which makes the materials suitable for upcoming lightweight and cutting-edge devices. The findings of this study hold significant promise for advancing the development of practical energy storage devices. This study

indicates that the materials support efficient and sustained energy storage, mimicking the behavior of batteries in terms of charge transfer and retention. The demonstrated performance of the SSD, marked by high specific capacitance, excellent rate capability, and mechanical stability, highlights its suitability for applications in flexible and wearable electronics, where lightweight, reliable, and bendable energy sources are essential. Moreover, the rapid charge–discharge characteristics and long cycling life make these devices ideal for high-power applications, such as short-duration energy buffering and power backup systems. From a manufacturing perspective, the symmetric configuration simplifies fabrication and reduces costs, thereby facilitating scalable device integration. Such characteristics make these nanostructures particularly suitable for high-performance energy storage applications, where stable and reliable charge–discharge cycles are essential. Therefore, we conclude that our work provides a novel approach for creating affordable, efficient ESC devices and other power-source systems for the next generation. Looking forward, further research should focus on optimizing the electrode–electrolyte interface to enhance ion transport, exploring solid-state and gel-based electrolytes to improve safety and flexibility, and investigating the mechanical and electrochemical durability of these devices under real-world conditions.

Data availability

The data supporting this article has been included as part of the article.

Conflicts of interest

There are no conflicts to declare.

Acknowledgements

References

1 J. Gubbi, R. Buyya, S. Marusic and M. Palaniswami, Internet of Things (IoT): A vision, architectural elements, and future directions, *Future Gener. Comput. Syst.*, 2013, **29**, 1645–1660, DOI: **10.1016/j.future.2013.01.010**.

2 Y. Han, Y. Ge, Y. Chao, C. Wang and G. G. Wallace, Recent progress in 2D materials for flexible supercapacitors, *J. Energy Chem.*, 2018, **27**, 57–72, DOI: **10.1016/j.jechem.2017.10.033**.

3 Y. Xie, T. M. Chou, W. Yang, M. He, Y. Zhao, N. Li and Z. H. Lin, Flexible thermoelectric nanogenerator based on the MoS2/graphene nanocomposite and its application for a self-powered temperature sensor, *Semicond. Sci. Technol.*, 2017, **32**(4), 044003, DOI: **10.1088/1361-6641/aa62f2**.

4 Y. P. Gao, X. Wu, K. J. Huang, L. L. Xing, Y. Y. Zhang and L. Liu, Two-dimensional transition metal diseleniums for energy storage application: a review of recent developments, *CrystEngComm*, 2017, **19**, 404–418, DOI: **10.1039/c6ce02223e**.

5 C. V. V. Muralee Gopi, R. Vinodh, S. Sambasivam, I. M. Obaidat and H.-J. Kim, Recent progress of advanced energy storage materials for flexible and wearable supercapacitor: From design and development to applications, *J. Energy Storage*, 2020, **27**, 101035, DOI: **10.1016/j.est.2019.101035**.

6 Y. Wang, X. Wu, Y. Han and T. Li, Flexible supercapacitor: Overview and outlooks, *J. Energy Storage*, 2021, **42**, 103053, DOI: **10.1016/j.est.2021.103053**.

7 H. Kelly-Holmes, *Advertising as Multilingual Communication*, Palgrave Macmillan UK, London, 2005, DOI: **10.1057/9780230503014**.

8 K. S. Kumar, N. Choudhary, Y. Jung and J. Thomas, Recent Advances in Two-Dimensional Nanomaterials for Supercapacitor Electrode Applications, *ACS Energy Lett.*, 2018, **3**, 482–495, DOI: **10.1021/acsenergylett.7b01169**.

9 P. He, M.-S. Cao, W.-Q. Cao and J. Yuan, Developing MXenes from Wireless Communication to Electromagnetic Attenuation, *Nano-Micro Lett.*, 2021, **13**, 115, DOI: **10.1007/s40820-021-00645-z**.

10 Y. P. Gao, K. J. Huang, H. L. Shuai and L. Liu, Synthesis of sphere-feature molybdenum selenide with enhanced electrochemical performance for supercapacitor, *Mater. Lett.*, 2017, **209**, 319–322, DOI: **10.1016/j.matlet.2017.08.044**.

11 X. Li, X. Xiao, Q. Li, J. Wei, H. Xue and H. Pang, Metal (M = Co, Ni) phosphate based materials for high-performance supercapacitors, *Inorg. Chem. Front.*, 2018, **5**, 11–28, DOI: **10.1039/c7qi00434f**.

12 A. Burk, Ultracapacitors: why, how, and where is the technology, *J. Power Sources*, 2000, **91**, 37–50.

13 Y.-P. Gao, K.-J. Huang, H.-L. Shuai and L. Liu, Synthesis of sphere-feature molybdenum selenide with enhanced electrochemical performance for supercapacitor, *Mater. Lett.*, 2017, **209**, 319–322, DOI: **10.1016/j.matlet.2017.08.044**.

14 K. J. Huang, J. Z. Zhang and Y. Fan, Preparation of layered MoSe2 nanosheets on Ni-foam substrate with enhanced supercapacitor performance, *Mater. Lett.*, 2015, **152**, 244–247, DOI: **10.1016/j.matlet.2015.03.130**.

15 M. Zhao, Q. Zhao, B. Li, H. Xue, H. Pang and C. Chen, Recent progress in layered double hydroxide based materials for electrochemical capacitors: Design, synthesis and performance, *Nanoscale*, 2017, **9**, 15206–15225, DOI: **10.1039/c7nr04752e**.

16 K. S. Bhat and H. S. Nagaraja, Effect of isoelectronic tungsten doping on molybdenum selenide nanostructures and their graphene hybrids for supercapacitors, *Electrochim. Acta*, 2019, **302**, 459–471, DOI: **10.1016/j.electacta.2019.02.059**.

17 X. Zhu, Z. Feng, L. Fan, Q. Wang, Y. Wei, L. Zhu, N. Li and Q. Zhang, Tailoring the morphologies of molybdenum selenides with improving their electrochemical

performances for supercapacitors, *J. Energy Storage*, 2024, **89**, 1–9, DOI: **10.1016/j.est.2024.111671**.

18 F. Ma, J. Lu, L. Pu, W. Wang and Y. Dai, Construction of hierarchical cobalt-molybdenum selenide hollow nanospheres architectures for high performance battery-supercapacitor hybrid devices, *J. Colloid Interface Sci.*, 2020, **563**, 435–446, DOI: **10.1016/j.jcis.2019.12.101**.

19 S. Tanwar, N. Singh and A. L. Sharma, Structural and electrochemical performance of carbon coated molybdenum selenide nanocomposite for supercapacitor applications, *J. Energy Storage*, 2022, **45**, 103797, DOI: **10.1016/j.est.2021.103797**.

20 G. Tang, W. Tang, Q. Li, B. Tian, X. Zhang, J. Liang and W. Wu, Boosting the Electrical Transfer by Molybdenum Doping for Robust and Flexible NiSe-Based Supercapacitor, *Small*, 2024, 2402609, DOI: **10.1002/smll.202402609**.

21 K. H. Park and M. Dhayal, Simultaneous growth of rutile TiO_2 as 1D/3D nanorod/nanoflower on FTO in one-step process enhances electrochemical response of photoanode in DSSC, *Electrochem. Commun.*, 2014, **49**, 47–50, DOI: **10.1016/j.elecom.2014.09.011**.

22 J. Deng, Z. Zhou, J. Chen, Z. Cheng, J. Liu and Z. Wang, Vanadium-Doped Molybdenum Diselenide Atomic Layers with Room-Temperature Ferromagnetism, *ChemPhysChem*, 2022, **23**(16), e202200162, DOI: **10.1002/cphc.202200162**.

23 P. Pazhamalai, K. Krishnamoorthy, S. Sahoo and S. J. Kim, Two-dimensional molybdenum diselenide nanosheets as a novel electrode material for symmetric supercapacitors using organic electrolyte, *Electrochim. Acta*, 2019, **295**, 591–598, DOI: **10.1016/j.electacta.2018.10.191**.

24 S. Tanwar, A. Arya and A. L. Sharma, $MoSe_2$-FeOOH nanocomposite as hybrid electrode material for high-performance symmetric supercapacitor, *Mater. Res. Bull.*, 2023, **160**, 112144, DOI: **10.1016/j.materresbull.2022.112144**.

25 V. K. Mariappan, K. Krishnamoorthy, P. Pazhamalai, S. Sahoo and S. J. Kim, Electrodeposited molybdenum selenide sheets on nickel foam as a binder-free electrode for supercapacitor application, *Electrochim. Acta*, 2018, **265**, 514–522, DOI: **10.1016/j.electacta.2018.01.075**.

26 P. Sivakumar, D. Vikraman, C. J. Raj, S. Hussain, J. Park, H. Kim and H. Jung, Hierarchical NiCo/NiO/NiCo2O4 composite formation by solvothermal reaction as a potential electrode material for hydrogen evolutions and asymmetric supercapacitors, *Int. J. Energy Res.*, 2021, **45**, 19947–19961, DOI: **10.1002/er.7065**.

27 S. Upadhyay and O. P. Pandey, Synthesis of layered 2H-$MoSe_2$ nanosheets for the high-performance supercapacitor electrode material, *J. Alloys Compd.*, 2021, **857**, 157522, DOI: **10.1016/j.jallcom.2020.157522**.

28 B. Kirubasankar, S. Vijayan and S. Angaiah, Sonochemical synthesis of a 2D-2D $MoSe_2$/graphene nanohybrid electrode material for asymmetric supercapacitors, *Sustainable Energy Fuels*, 2019, **3**, 467–477, DOI: **10.1039/c8se00446c**.

29 J. Qu, Y. Bai, X. Li, K. Song, S. Zhang, X. Wang, X. Wang and S. Dai, Rational design of NiSe2@rGO nanocomposites for advanced hybrid supercapacitors, *J. Mater. Res. Technol.*, 2021, **15**, 6155–6161, DOI: **10.1016/j.jmrt.2021.11.036**.

30 K. S. Velu, S. Mohandoss, Y. R. Lee and J. H. Seo, Fabrication of a flexible asymmetric supercapacitor using molybdenum selenide and titanium carbide MXene ($MoSe_2$@$Ti_3C_2T_x$) nanocomposite on carbon cloth, *Ceram. Int.*, 2025, **51**, 13782–13796, DOI: **10.1016/j.ceramint.2025.01.213**.

31 Y. Li, Y. Sun, S. Zhang, X. Wu, M. Song, M. Jiao, Q. Qin and L. Mi, Self-assembled molybdenum disulfide nanoflowers regulated by lithium sulfate for high performance supercapacitors, *RSC Adv.*, 2023, **13**, 26509–26515, DOI: **10.1039/d3ra04852g**.